Mon. Not. R. Astron. Soc. **381,** 41–51 (2007) doi:10.1111/j.1365-2966.2007.12249.x

The evolution of dark matter halo properties in clusters, filaments, sheets and voids

Oliver Hahn,[1⋆] C. Marcella Carollo,[1] Cristiano Porciani[1] and Avishai Dekel[2]
[1]*ETH Zürich, 8093 Zürich, Switzerland*
[2]*Racah Institute of Physics, The Hebrew University, Jerusalem 91904, Israel*

Accepted 2007 July 18. Received 2007 July 18; in original form 2007 March 22

ABSTRACT

We use a series of high-resolution *N*-body simulations of the concordance cosmology to investigate the redshift evolution since $z = 1$ of the properties and alignment with the large-scale structure (LSS) of haloes in clusters, filaments, sheets and voids. We find that (i) once a rescaling of the halo mass with $M_*(z)$, the typical mass scale collapsing at redshift z, is performed, there is no further significant redshift dependence in the halo properties; (ii) the environment influences the halo shape and formation time at all investigated redshifts for haloes with masses $M \lesssim M_*$ and (iii) there is a significant alignment of both spin and shape of haloes with filaments and sheets. In detail, at all redshifts up to $z = 1$: (a) haloes with masses below $\sim M_*$ tend to be more oblate when located in clusters than in the other environments; this trend is reversed at higher masses: above about M_*, haloes in clusters are typically more prolate than similar massive haloes in sheets, filaments and voids. (b) The haloes with $M \gtrsim M_*$ in filaments spin more rapidly than similar mass haloes in clusters; haloes in voids have the lowest median spin parameters. (c) Haloes with $M \lesssim M_*$ tend to be younger in voids and older in clusters. (d) In sheets, halo spin vectors tend to lie preferentially within the sheet plane independent of halo mass; in filaments, instead, haloes with $M \lesssim M_*$ tend to spin parallel to the filament and higher mass haloes perpendicular to it. For halo masses $M \gtrsim M_*$, the major axis of haloes in filaments and sheets is strongly aligned with the host filament or the sheet plane, respectively. Such halo–LSS alignments may be of importance in weak lensing analyses of cosmic shear. A question that is opened by our study is why, in the $0 < z < 1$ redshift regime that we have investigated, the mass scale for gravitational collapse, M_*, sets roughly the threshold below which the LSS environment either begins to affect, or reverses, fundamental properties of dark matter haloes.

Key words: methods: *N*-body simulations – galaxies: haloes – cosmology: theory – dark matter – large-scale structure of Universe.

1 INTRODUCTION

Numerical simulations of concordance cosmology have shown that properties of dark matter haloes do not depend only on the mass of the halo, as suggested by prior analytical work based on the excursion set theory for structure evolution (e.g. Bond et al. 1991; Lacey & Cole 1993). Rather, they also depend on the environment in which the halo resides (e.g. Gao, Springel & White 2005; Harker et al. 2006; Wechsler et al. 2006; Hahn et al. 2007, hereafter Paper I; Wang, Mo & Jing 2007). This dependence on environment is quite significant at redshift zero for low-mass haloes, typically with masses $<5 \times 10^{12}\, h^{-1}\, \mathrm{M}_\odot$. In detail, using marked statistics, Sheth & Tormen (2004) find evidence that haloes of a given mass form earlier in dense regions. High-resolution simulations confirm this finding and quantify it as a function of halo mass (Gao et al. 2005; Harker et al. 2006; Croton, Gao & White 2007; Maulbetsch et al. 2007; Reed et al. 2007). At the same time it has become clear that also other halo properties as concentration and spin correlate with local environment (Avila-Reese et al. 2005; Wechsler et al. 2006; Bett et al. 2007; Paper I; Macciò et al. 2007; Wetzel et al. 2007). Gao & White (2007) find that haloes with e.g. high spin parameter or formation time tend to be more strongly clustered than younger and low-spin haloes. It is possible that this environmental dependence of halo properties has also an impact on the baryonic galaxies. Galaxy properties in the local Universe are known to vary systematically with environment (e.g. Dressler 1980; Kauffmann et al. 2004; Blanton et al. 2005).

⋆E-mail: hahn@phys.ethz.ch

In this paper, we extend the investigation of the properties of dark matter haloes as a function of environment to high redshifts. In particular, we follow the definition of environment that we presented in Paper I, which associates haloes to four classes with different dynamical properties: voids, sheets, filaments and clusters. These four environments are identified on the basis of a tidal stability criterion for test particles which is inspired by the Zel'dovich approximation (Zel'dovich 1970). We find that, at each redshift, all investigated properties of haloes show some correlation with mass and environment, and that the redshift dependence of halo properties with mass is removed when such properties are investigated as a function of the rescaled mass M/M_*, where M_* is the typical mass scale collapsing at each epoch.

The paper is organised as follows. In Section 2, we briefly summarize the specifics of our N-body simulations, the definitions of the halo properties that we study and the definitions of the four environments – clusters, sheets, filaments and voids. We present the results in Section 3 and summarize our conclusions in Section 4.

2 NUMERICAL SIMULATIONS AND DEFINITIONS

We use the three high-resolution cosmological N-body simulations described in more detail in Paper I, which were obtained with the tree-PM code GADGET-2 (Springel 2005). These simulations are used to follow the formation and evolution of large-scale structure (LSS) in a flat Λ cold dark matter (ΛCDM) cosmology with matter density parameter $\Omega_\mathrm{m} = 0.25$, baryonic contribution $\Omega_\mathrm{b} = 0.045$ and a present-day value of the Hubble constant $H_0 = 100\,h\,\mathrm{km\,s^{-1}\,Mpc^{-1}}$ with $h = 0.73$ with an initial power spectrum normalized to have $\sigma_8 = 0.9$. Each simulation consists of 512^3 collisionless dark matter particles in periodic boxes of sizes $L_1 = 45\,h^{-1}$ Mpc, $L_2 = 90\,h^{-1}$ Mpc and $L_3 = 180\,h^{-1}$ Mpc, respectively. The corresponding particle masses are 4.7×10^7, 3.8×10^8 and $3.0 \times 10^9\,h^{-1}\,\mathrm{M}_\odot$ for the three boxes. Initial conditions were generated using the GRAFIC2 tool (Bertschinger 2001). Particle positions and velocities were saved for 30 time-steps, logarithmically spaced in expansion parameter a between $z = 10$ and 0. The mass range of these three simulations allows us to resolve haloes with masses below M_* up to redshifts $z \lesssim 1$.

The halo properties that we investigate are formation redshift, shape and spin parameter. The formation redshift and shape parameters are defined as in Paper I; we adopt, however, a slightly different approach to measure the halo spin parameter than in our previous work. We summarize our definitions below.

2.1 Halo catalogues

Haloes were identified in each snapshot using the standard friends-of-friends (FOF; Davis et al. 1985) algorithm with a linking length equal to 0.2 times the mean interparticle distance. Haloes that are well resolved in each of the three simulations are then combined into one single catalogue. Unrelaxed systems were identified and deleted from the halo catalogues. These unrelaxed systems are mainly contributed by close-pair halo configurations which are spuriously linked into one single halo. To identify them, we follow Bett et al. (2007) and define the virialization parameter

$$\alpha \equiv \frac{2K}{V} + 1, \tag{1}$$

where K is the total kinetic energy including the Hubble flow with respect to the centre of mass and V is the total potential energy of the isolated FOF halo. The potential is computed using a tree for groups with more than 5000 particles, and via direct summation for smaller haloes. The virial theorem states that the time average of α vanishes for any isolated relaxed object. However, infalling material exerts a surface pressure such that $\alpha \lesssim 0$ (Hetznecker & Burkert 2006). In addition, structures that are gravitationally bound have $\alpha > -3$. In order to exclude accidentally linked unvirialized structures or haloes that are just about to merge, it suffices to fix bounds on α. In order to directly compare with Bett et al. (2007), we make the same choice of $|\alpha| < 1/2$ that was adopted by those authors to set the threshold between virialized and non-virialized structures.

Finally, we also exclude from our halo catalogues all those structures where the distance between the centre of mass $\boldsymbol{r}_\mathrm{CM}$ and the most bound particle $\boldsymbol{r}_\mathrm{MB}$ exceeds a fixed fraction $f = 0.25$ of the largest distance between a particle in the halo and the centre of mass $\boldsymbol{r}_\mathrm{max}$, i.e. $f = |\boldsymbol{r}_\mathrm{CM} - \boldsymbol{r}_\mathrm{MB}|/|\boldsymbol{r}_\mathrm{max}|$.

The cleaning of the halo catalogues has a strong effect on the spin parameter distribution but only a minor influence on the other quantities that we study in this paper.

2.2 Formation redshift

For each halo at redshift z, we identify a progenitor at $z_\mathrm{p} > z$ by identifying particles that are contained in both haloes. The main progenitor is then chosen to be the most massive halo at each redshift that contributes at least 50 per cent of its particles to the final halo. We then define the formation redshift z_form to be the epoch at which a main progenitor which has at least half of the final mass first appears in the simulation; specifically, z_form is found by linearly interpolating between simulation snapshots in $\log z$ to find the point where half of the given halo mass is accumulated.

2.3 Halo shape

In order to determine the shape of haloes, we use the moment of inertia tensor

$$I_{jk} \equiv m \sum_i \left(r_i^2 \delta_{jk} - x_{i,j} x_{i,k}\right), \tag{2}$$

where m is the particle mass, $r_i \equiv |(x_{i,1}, x_{i,2}, x_{i,3})|$ is the distance of the ith particle from the centre of mass of the halo and δ_{jk} denotes the Kronecker symbol. Given the lengths of the principal axes of inertia $l_1 \geqslant l_2 \geqslant l_3$, we then use the following definitions of sphericity S and triaxiality T:

$$S = \frac{l_3}{l_1} \qquad \text{and} \qquad T = \frac{l_1^2 - l_2^2}{l_1^2 - l_3^2}. \tag{3}$$

We find that a minimum of 500 particles per halo guarantees numerically reliable estimates of the shape parameters.

2.4 Halo spin parameter

We estimate the spin parameter (Peebles 1969) of a halo using the simplified form (Bullock et al. 2001)

$$\lambda' \equiv \frac{|\boldsymbol{J}_\mathrm{vir}|}{\sqrt{2} M_\mathrm{vir} V_\mathrm{vir} R_\mathrm{vir}}. \tag{4}$$

Here all quantities with the subscript 'vir' (angular momentum, mass and circular velocity) are computed within a sphere of radius R_vir around the most bound particle enclosing a mean density of $\Delta(z)\rho_\mathrm{c}(z)$, where $\rho_\mathrm{c}(z)$ is the critical density, and $\Delta(z)$ the density

parameter according to the spherical collapse model. This density parameter can be approximated by (Bryan & Norman 1998)

$$\Delta(z) = 18\,\pi^2 + 82\,f(z) - 39\,f^2(z), \tag{5}$$

with

$$f(z) = \frac{-\Omega_\Lambda}{\Omega_\mathrm{m}\,(1+z)^3 + \Omega_\Lambda} \tag{6}$$

in a flat cosmology. Under the assumption that the halo is in dynamical equilibrium, $V_\mathrm{vir}^2 = GM_\mathrm{vir}/R_\mathrm{vir}$, the spin parameter can be rewritten as

$$\lambda' = \frac{|\boldsymbol{J}_\mathrm{vir}|}{\sqrt{2GR_\mathrm{vir}}M_\mathrm{vir}^{3/2}}. \tag{7}$$

Systematic numerical artefacts were found to be negligible for haloes consisting of at least 300 particles. The cleaning of the halo catalogues, as described in Section 2.1, has a strong influence on the distribution of λ'. The probability for two haloes of similar mass to be erroneously linked by the halo finder grows both with the environmental density and decreasing mass of the haloes. This leads to an increasing component of unrelaxed structures of low mass in the spin distribution for which the virialization conditions are not fulfilled. Furthermore, the angular momentum $\boldsymbol{J}$ is dominated by the orbital angular momentum of the pair rather than the intrinsic spin of either one of them. Exclusion of unrelaxed objects removes the tail of these apparent high-spin haloes with $\lambda' \gtrsim 0.1$.

2.5 Environmental classification

We employ the definition of environment that was described in detail in Paper I. This classification is based on a local stability criterion for the orbits of test particles in the matter distribution at a fixed epoch. A series expansion of the equation of motion for a test particle in the smoothed matter distribution gives a zero-order acceleration and a first-order deformation term that is determined by the tidal field tensor, i.e. the Hessian of the peculiar gravitational potential. We then classify the contraction/expansion behaviour of this first-order term by the number of its positive/negative eigenvalues. In analogy with Zel'dovich theory (Zel'dovich 1970), the application of this criterion provides four environmental categories defined by the signs of the three eigenvalues $\lambda_1 \leqslant \lambda_2 \leqslant \lambda_3$, namely:

(i) clusters ($\lambda_{1,2,3} \geqslant 0$),
(ii) filaments ($\lambda_{2,3} \geqslant 0$, $\lambda_1 < 0$),
(iii) sheets ($\lambda_3 \geqslant 0$, $\lambda_{1,2} < 0$) and
(iv) voids ($\lambda_{1,2,3} < 0$).

This definition relies on one free parameter, the length scale R_s of the Gaussian filter that is used to smooth the matter distribution before obtaining the gravitational potential on a grid. As done in Paper I, we fix the smoothing scale at redshift $z = 0$ to be $R_\mathrm{s} = 2.1\,h^{-1}$ Mpc, as this value provides the best agreement between the outcome of the orbit-stability criterion and our a posteriori visual classification of the different environments. The smoothing length scale R_s is related to the mass M_s contained in the Gaussian filter at mean density $\bar\rho$ via $M_\mathrm{s} = (2\pi)^{3/2}\bar\rho R_\mathrm{s}^3$; thus, a smoothing scale $R_\mathrm{s} = 2.1\,h^{-1}$ Mpc corresponds to $M_\mathrm{s} = 10^{13}\,h^{-1}\,\mathrm{M}_\odot$.

A natural mass scale at any given redshift is given by the typical mass scale for collapse $M_*(z)$ defined as follows. A spherical top-hat perturbation collapses when its linear overdensity exceeds a value of $\delta_\mathrm{c} = 1.686$ with only a weak dependence on cosmological parameters (e.g. Eke, Cole & Frenk 1996). The variance of linear density fluctuations at a given mass scale M is related to the linear power spectrum $P(k, z)$ at redshift z by

$$\sigma^2(M, z) = \frac{1}{2\pi^2}\int_0^\infty \mathrm{d}k\,k^2\,P(k, z)\,\widetilde{W}_\mathrm{TH}^2(k, M), \tag{8}$$

where $\widetilde{W}_\mathrm{TH}(k, M)$ is the Fourier transform of a spherical top-hat window function of comoving size $R = (3M/4\pi\bar\rho)^{1/3}$, and $\bar\rho$ is the comoving mean mass density of the universe. At a given redshift, the typical mass scale $M_*(z)$ to collapse from a 1σ fluctuation is hence given by the implicit solution of

$$\sigma(M_*, z) = \delta_\mathrm{c}. \tag{9}$$

The mass scale $M_*(z)$ at $z = 0$ is $5.5 \times 10^{12}\,h^{-1}\,\mathrm{M}_\odot$.

When computing the environmental classification at redshifts $z > 0$, there are two possible approaches that can be followed: (i) to keep the smoothing scale R_s (M_s) fixed to the $z = 0$ value: the environment is thus defined over typical separations of a few Mpc in comoving space or (ii) to vary the smoothing scale. In particular, a natural choice for a redshift-dependent smoothing scale is to maintain the ratio M_s/M_* fixed for the Gaussian filter. The respective mass scales $M_*(z)$ for the high-z simulation snapshots investigated in this paper, i.e. $z = 0.49$ and 1.05, are 1.2×10^{12} and $1.9 \times 10^{11}\,h^{-1}\,\mathrm{M}_\odot$. Fixing the ratio M_s/M_* maintains the smoothing on scales of order $\sim 2M_*$ at all redshifts.

The resulting classifications for both $M_\mathrm{s} = $ const. and $M_\mathrm{s}/M_* = $ const. at redshifts $z = 0$, 0.49 and 1.05 are shown in Fig. 1 using different colours for the cluster, sheet, filament and void environments. We observe some differences between the two smoothing approaches. With a fixed smoothing length $R_\mathrm{s} = $ const., shown in panels (b) and (d), the regions classified as voids, sheets and filaments remain virtually unchanged since $z = 1$, while the cluster environments grow substantially in size, from $z = 0$ to higher redshifts, and extend well into the filaments at $z = 1$. With the constant M_s/M_* smoothing, shown in panels (c) and (e), a much larger number of individual haloes change environment with redshift: at the resolution of our simulations, very few haloes are detected at $z = 1$ in void regions, while many haloes are associated at the same redshift to relatively small cluster environments. In Tables 1 (for fixed M_s) and 2 (for fixed M_s/M_*) we show the fraction of haloes at $z = 0$ that change their environmental class from $z = 1.05$ through 0.49 to $z = 0$ by following the main progenitors of each halo with a minimum mass of $10^{11}\,h^{-1}\,\mathrm{M}_\odot$ in the $90\,h^{-1}$ Mpc box. For a fixed smoothing mass scale, indeed less haloes change their environmental class as the density contrasts between the environments grow through gravitational collapse.

The fraction of volume attributed to each of the four environments as a function of redshift is shown for both smoothing approaches in Fig. 2. For a fixed smoothing mass $M_\mathrm{s} = $ const., the density field asymptotically approaches Gaussianity with increasing redshift and thus the expected volume fractions for the four environments (cf. Doroshkevich 1970). The behaviour is very different with the constant M_s/M_* smoothing. The volume occupied by the unstable structures (sheets and voids) increases with redshift, while the volume fractions of the stable structures (clusters and filaments) decrease compared to the values at $z = 0$.

The redshift evolution of the median value of the smoothed overdensity field as measured at the centres of haloes in the four environments is shown in Fig. 3. For a constant smoothing scale, the median overdensities grow faster than expected in linear perturbation theory as $|\delta| \gtrsim 1$ in clusters and voids. With the $M_\mathrm{s}/M_* = $ const. smoothing, however, the median overdensities are found to be essentially constant at all redshifts. In both smoothing approaches, the

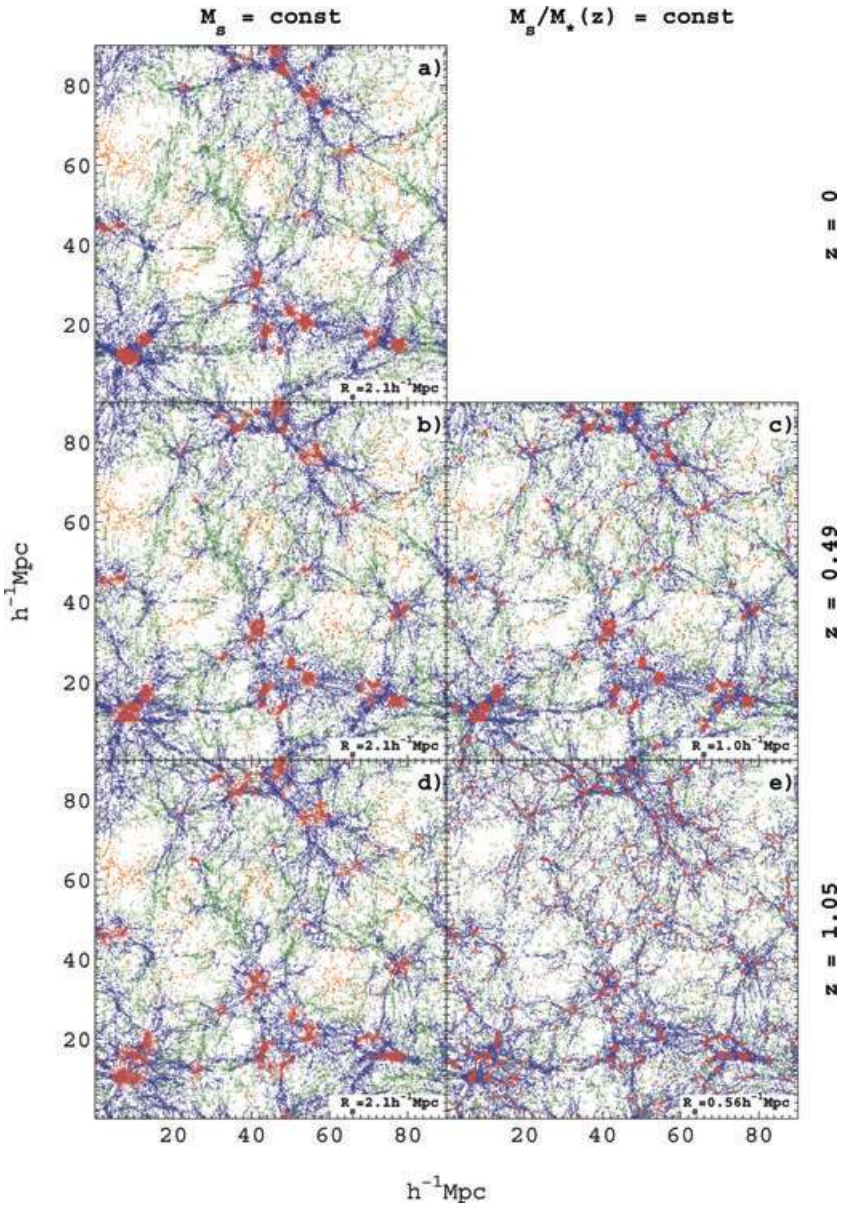

Figure 1. Halo environment classification as a function of redshift in projected slices of $15\,h^{-1}$ Mpc for the $90\,h^{-1}$ Mpc box. Only for presentation purposes, i.e. to increase the contrast in the figure, we represent with a dot haloes down to structures with only 10 particles. The four environments are identified by colour: voids (orange), sheets (green), filaments (blue) and clusters (red). Panel (a) is the slice at $z = 0$; the smoothing mass scale is $M_s = 10^{13}\,h^{-1}\,M_\odot$. Panels (b) and (c) are snapshots at $z = 0.49$; panels (c) and (d) are at $z = 1.05$. In panels (b) and (d) the smoothing scale M_s adopted for the environmental classification is as at $z = 0$; in panels (c) and (e) it is the ratio M_s/M_* that is kept fixed.

median overdensity in filaments is constant. The median overdensities, smoothed on scales of $R_s = 2.1\,h^{-1}$ Mpc at redshift zero, are $\delta = -0.79$, -0.55, 0.28 and 4.44 in voids, sheets, filaments and clusters, respectively.

We note that with both smoothing approaches, and most relevantly when adopting a constant M_s/M_* ratio for the smoothing, the haloes in the immediate surroundings of the clusters at $z = 1$ are classified as filaments/sheets at this redshift, but they make the transition to the cluster environment by $z = 0$. This allows us to rigorously identify, and thus study the properties of, the haloes in these intermediate-density 'transition regions', before their ultimate migration into the deeper potential wells of rich clusters at $z = 0$. We plan to investigate these haloes in future work.

3 THE REDSHIFT EVOLUTION OF HALO PROPERTIES IN DIFFERENT ENVIRONMENTS

3.1 Mass functions

The choice of smoothing scale with redshift has an impact on the analysis of the redshift evolution of the halo properties in the different environments. Starting with the halo mass functions, shown in Fig. 4 for the cluster, sheet, filament and void environments at $z = 0$, 0.49 and 1.05, there is a substantial change in their shapes when using one or the other of the smoothing approaches. Adopting a constant M_s/M_* for the smoothing scale leads to a substantial increase

Table 1. Environmental transition matrix for the main progenitor branch of haloes with masses $M(z=0) > 10^{11}\,h^{-1}\,\mathrm{M}_\odot$ between $z=0$ and 0.49 (upper half) and $z=1.05$ (lower half). Matrix entries are given in per cent of the total number of haloes at $z=0$. Non-diagonal elements represent haloes that change classification. Environment is determined with $M_\mathrm{s}=$ const. (i.e. $R_\mathrm{s}=2.1\,h^{-1}$ Mpc at all redshifts).

		$z=0.49$		
$z=0$	Void	Sheet	Filament	Cluster
Void	1.0	0.094	0	0
Sheet	0.28	27	1.1	0
Filament	0	5.5	54	0.29
Cluster	0	0.088	6.4	4.2
		$z=1.05$		
Void	0.95	0.18	0	0
Sheet	0.56	26	1.86	0
Filament	0.028	10.3	49	0.46
Cluster	0	0.53	7.5	2.7

Table 2. As Table 1, but with the environment now determined adopting $M_\mathrm{s}/M_* =$ const.

		$z=0.49$		
$z=0$	Void	Sheet	Filament	Cluster
Void	0.34	0.71	0.077	0
Sheet	0.050	18	9.9	0.36
Filament	0	6.2	51	2.9
Cluster	0	0.31	8.0	2.4
		$z=1.05$		
Void	0	0.22	0.79	0.12
Sheet	0	5.0	19	4.1
Filament	0	4.5	46	8.8
Cluster	0	0.72	8.0	2.0

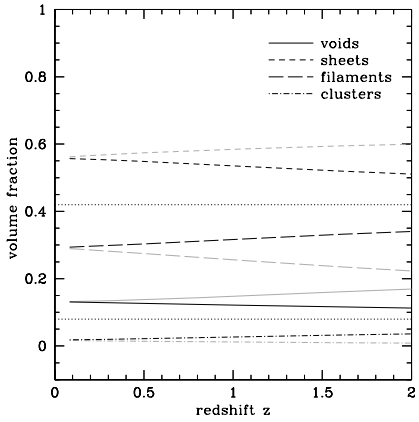

Figure 2. Volume fractions for the $90\,h^{-1}$ Mpc box over redshift. Thick black lines represent the fractions obtained using a smoothing scale constant with redshift, and grey lines indicate the corresponding fractions obtained when keeping the ratio M/M_* constant. Thin dotted black lines represent the values predicted for a Gaussian field (42 per cent for sheets and filaments, and 8 per cent for voids and clusters).

in low-mass haloes that are classified to be in clusters relative to the other environments. In voids, sheets and high-mass filaments, the mass functions are higher when smoothing with $M_\mathrm{s}=$ const. than when adopting a constant M_s/M_* ratio; the trend reverses for haloes

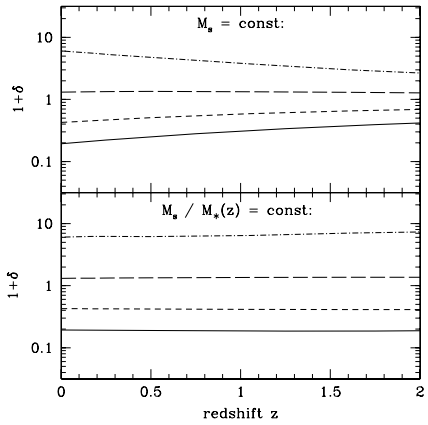

Figure 3. Median overdensity in cluster (dot–dashed), filament (long dashed), sheet (short dashed) and void (solid) environments for a constant smoothing scale M_s (top) and for a constant ratio M_s/M_* (bottom) with redshift. The smoothing scale at redshift zero is $M_\mathrm{s}=10^{13}\,h^{-1}\,\mathrm{M}_\odot$.

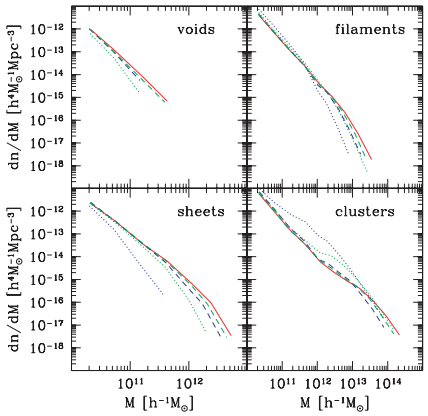

Figure 4. Mass function of the haloes residing in voids, sheets, filaments and clusters at redshifts $z=0$ (red), $z=0.49$ (green) and $z=1.05$ (blue). Abundances in the whole box have been rescaled by the corresponding volume fractions. The dotted curves are obtained with $M_\mathrm{s}/M_*=$ const., the dashed curves with $M_\mathrm{s}=$ const. at $z>0.49$ and 1.05. The smoothing scale at redshift zero is $M_\mathrm{s}=10^{13}\,h^{-1}\,\mathrm{M}_\odot$; here the two smoothings coincide and are represented by the solid line.

in low-mass filaments and clusters, for which the mass functions are instead enhanced when using the $M_\mathrm{s}/M_*=$ const. smoothing scale. The inflexion point on scales of $\sim 10^{12}\,h^{-1}\,\mathrm{M}_\odot$ ($\sim 10^{12.5}\,h-1\,\mathrm{M}_\odot$) in the mass function of $z=1.05$ ($z=0.49$) clusters for the $M_\mathrm{s}/M_*=$ const. smoothing reflects the increasing abundance with redshift of isolated small clusters that we mention in Section 2.5. At all redshifts of our study, the clusters have the highest mean number density of haloes, followed by filaments, sheets and voids, respectively.

3.2 Halo formation redshift

A closer inspection of the dependence of halo properties on the adopted smoothing scale shows that, with both approaches, there is always a threshold mass scale M_t below which the environmental influence on halo properties either switches sign or transitions from being negligible to becoming increasingly more substantial with decreasing halo mass, down to the $\sim 10^{10}\,h^{-1}\,\mathrm{M}_\odot$ scales which can be probed with our simulations. Fig. 5 shows, for both smoothing

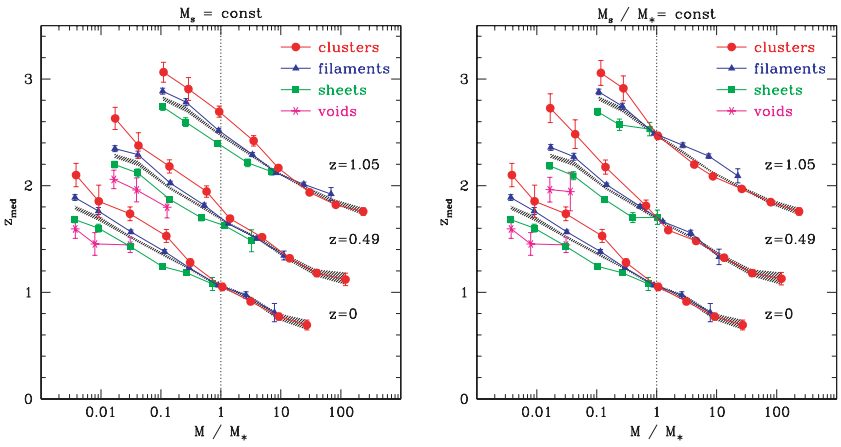

Figure 5. Median formation redshift in voids, sheets, filaments and clusters as a function of halo mass in units of $M_*(z)$ at redshifts $z = 0$, 0.49 and 1.05. The left-hand panel shows the results when smoothing with a constant M_s; the right-hand panel shows the case of the smoothing with a constant M_s/M_* ratio. Error bars indicate the uncertainty on the median. The shaded area indicates the 1σ confidence area for the median of the whole sample not split by environment.

approaches, the dependence on environment and mass (in units of M_*) of the median halo formation redshift $z_{\rm med}$. Error bars are estimates of the error in the median, and are computed as

$$\Delta x = \frac{x_{0.84} - x_{0.16}}{\sqrt{N_{\rm h}}}, \tag{10}$$

where $N_{\rm h}$ is the number of haloes used to sample the distribution of x, and $x_{0.84}$ and $x_{0.16}$ denote the 84th and 16th percentile of the distribution. These values would correspond to 1σ errors if the underlying distribution were Gaussian. The 1σ confidence region of the median formation redshift determined from all environments is represented by the shaded regions in Fig. 5. As discussed in Paper I, this overall behaviour, not split by environment, is well fit by a logarithmic relation over five decades in mass at $z = 0$. This relation reflecting hierarchical assembly is also present at higher redshifts. We fit a model of the form

$$z_{\rm med} = c_1 - c_2 \log_{10} \frac{M}{M_*(z)}. \tag{11}$$

A least-squares fit to all haloes extracted from our three simulation boxes provides the following parameters at the three redshifts:

$$\left.\begin{aligned} c_1 &= 1.07 \pm 0.01, \\ c_2 &= 0.30 \pm 0.01, \end{aligned}\right\} \quad z = 0,$$

$$\left.\begin{aligned} c_1 &= 1.70 \pm 0.01, \\ c_2 &= 0.33 \pm 0.01, \end{aligned}\right\} \quad z = 0.49,$$

$$\left.\begin{aligned} c_1 &= 2.47 \pm 0.01, \\ c_2 &= 0.34 \pm 0.01, \end{aligned}\right\} \quad z = 1.05.$$

We note that, in all plots and thus at all redshifts and for both smoothing approaches, there is indeed a mass scale $M_{\rm t}$ at which the curves for the four environments meet, indicating the vanishing of significant environmental influence above this mass threshold. Specifically, below $M_{\rm t}$, haloes form earlier in clusters than in filaments, followed by sheets and then voids. This difference in formation time increases with decreasing mass below the threshold $M_{\rm t}$.

It is clear from Fig. 5 that, in the case of a smoothing scale that remains constant with redshift, the threshold $M_{\rm t}$ coincides with the mass scale for gravitational collapse M_* at $z = 0$, but strongly departs (and increases relative to M_*) at higher redshifts. Interestingly, however, in the case of the $M_{\rm s}/M_* = $ const. smoothing scale, the threshold mass is easily identified to lie very close to M_* at all redshifts. This difference is simply due to the different association of haloes to the *cluster* and *filament* environments in the two smoothing approaches that is also observed in the mass functions (cf. Fig. 4). Furthermore, we note that the $z = 0.49$ and 1.05 relations are very similar to the one at $z = 0$, for which we had already provided the analytic fits with environment-dependent slopes for masses $M < M_*$ in Paper I. The environmental dependence of the halo formation redshifts below the M_* mass scale that we have found agrees with the analysis of Gao & White (2007), who find that haloes with higher formation redshifts are more strongly clustered.

Interestingly, at the highest redshift of our study ($z = 1.05$), and for the $M_{\rm s}/M_* = $ const smoothing, our simulations show that haloes with masses $M \gtrsim M_*$ in filaments tend to have earlier formation times than haloes of similar masses in the cluster environment, i.e. an opposite trend than the one observed at all redshifts below $M = M_*$.

The fact that, in the case of a fixed $M_{\rm s}/M_*$ smoothing ratio, the environmental dependence is explicitly seen to appear around $M/M_* = 1$, hints at a physical relevance of this scale in establishing the onset of the environmental dependence of halo properties at all redshifts. This motivates us to identify the constant $M_{\rm s}/M_*$ ratio as the more fundamental smoothing scale in our analysis, and thus to use this smoothing scale in the remainder of our study of the redshift evolution of halo spins, shapes and alignments as a function of environment.

3.3 Halo spin

Fig. 6 shows the median spin parameter $\lambda'_{\rm med}$ as a function of normalized mass M/M_* for haloes at $z = 0$, 0.49 and 1.05 in the cluster, sheet, filament and void environments. We also plot the results integrated over all environments (shaded region in Fig. 6), for comparison with previous studies. In agreement with these (e.g. Vitvitska et al. 2002), we do not observe any significant evolution of the global spin parameter with redshift. Our results also confirm a weak mass dependence of the median spin parameter as found at $z = 0$ by Bett et al. (2007), and furthermore extend this result to significantly lower masses. Integrated over all environments, the spin–mass relationship is weakly increasing up to $\approx 10 M_*(z)$, while the highest masses at each redshift have again a slightly smaller median spin parameter.

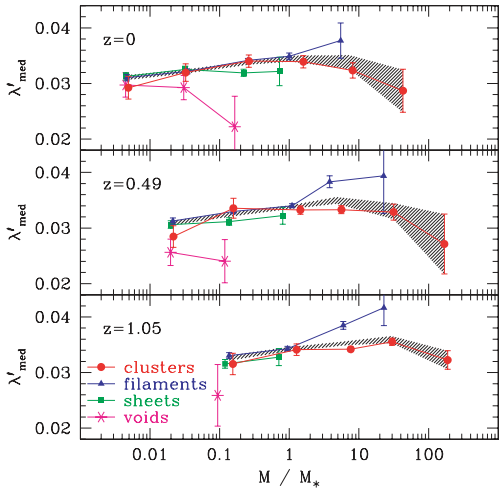

Figure 6. Median spin parameter in filaments and clusters as a function of halo mass in units of M_* at redshifts $z = 0$, 0.49 and 1.05. Error bars indicate the uncertainty on the median. The shaded grey area indicates the 1σ confidence area of the median of the whole sample not split by environment.

We find some dependence of the halo spin on environment at all redshifts of our analysis. More specifically, high-mass ($M > M_*$) haloes in filaments have a higher median spin at all redshifts than comparable-mass haloes in the cluster environments; in the voids, haloes with masses substantially below $M_*(z)$ spin systematically more slowly (i.e. median $\lambda' \lesssim 0.03$) than haloes of similar masses in any other environment. We have tested that this trend of void haloes having lower median spin parameters persists and actually increases when a larger scale is adopted for the smoothing, to optimize the identification of the void regions (cf. Paper I). At the lowest masses we do not observe any significant difference between haloes in clusters, filaments or sheets.

Gao & White (2007) report that, in their simulations, the most rapidly spinning haloes are more clustered than the slowest spinning haloes, which is in agreement with our earlier findings at $z = 0$ (Paper I). Our results, after removing unrelaxed haloes as described in Section 2.1, do not support a very strong correlation between environment and spin at low masses. Still, it is slightly more likely to find the most rapidly spinning objects in environments of higher median density.

3.4 Halo shape

In Fig. 7, we show the median sphericity and triaxiality of haloes in the four environments as a function of their mass for redshifts $z = 0$, 0.49 and 1.05. Independent of redshift and environment, haloes tend to be more spherical with decreasing mass. Over a large range of masses, haloes at $z = 1.05$ are however less spherical than haloes of similar mass at $z = 0$; Avila-Reese et al. (2005) and Allgood et al. (2006) find a similar result in their analyses. The mass–shape relations, expressed as scale-free functions of M/M_*, show no significant evolution with redshift up to $z \sim 1$; the fact that the entire redshift evolution of the shapes of haloes is driven by the evolution of the mass scale for gravitational collapse, M_*, is also supported by the independent studies quoted above.

Similarly to the $z = 0$ case (Bett et al. 2007; Paper I), the mass–sphericity and the mass–triaxiality relation of the global (i.e. not split for environment) sample follow a broken logarithmic relation also at high redshifts. The change in slope in these relationships occurs around $M \approx M_*$. We detect, however, a relatively small but systematic difference in the sphericity and triaxiality of $M < M_*$ haloes in low- and high-density environments, i.e. the slope in the $M \lesssim M_*$ regime weakly depends on the environment. Specifically, the median sphericity of $M < M_*(z)$ haloes decreases systematically from the cluster environments to the filaments, sheets and voids. At all redshifts, a weak trend is observed for haloes with masses below M_* to be more oblate in clusters than in filaments, and more prolate in sheets than in filaments; for haloes above M_*, there is a stronger evidence for haloes in filaments to be systematically more oblate than in clusters. These environmental differences at low masses are observed to be already in place at $z = 0.49$; the resolution of our simulations is not adequate to properly investigate these effects at $z = 1.05$ (minimum halo mass $\approx 0.1 M_*$).

3.5 Halo alignments

3.5.1 Halo–LSS alignment

Extending the analysis of Paper I to redshifts above zero, we use the directional information derived from the eigenstructure of the tidal field tensor to estimate the alignment of halo spin withthe

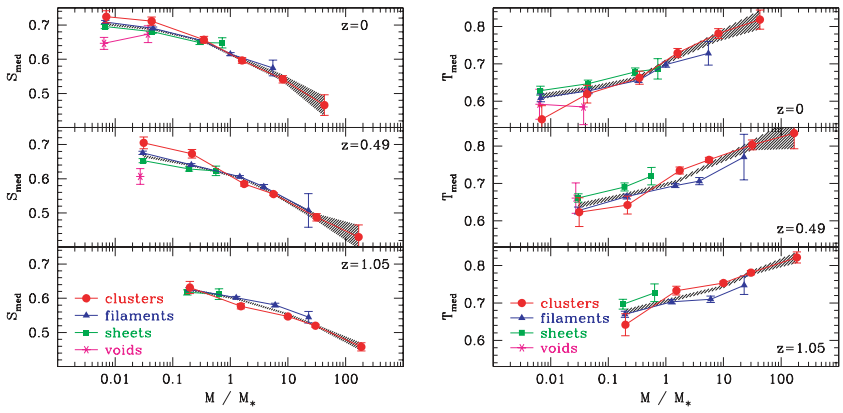

Figure 7. Median halo sphericity (left) and triaxiality (right) as a function of halo mass in units of M_* for haloes in the four environments at redshift $z = 0$, 0.49 and 1.05. Environment is defined adopting a constant M_s/M_* ratio. Error bars represent the error in the median. The shaded grey area indicates the 1σ confidence area of the median of the whole sample not split by environment.

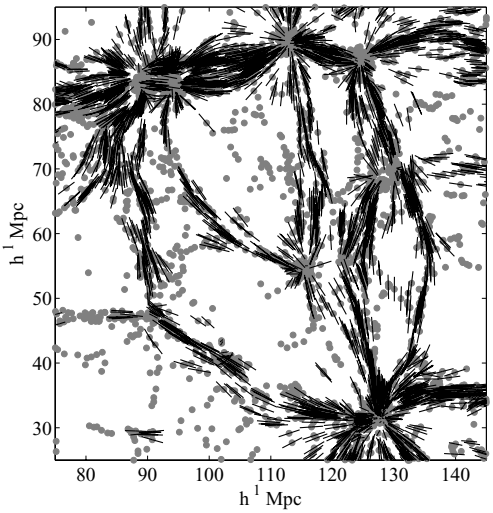

Figure 8. Unit eigenvectors indicating the direction of the filaments are shown in black for filament haloes in a slice of 8 h^{-1} Mpc in the 180 h^{-1} Mpc box at $z = 0$. The grey symbols indicate halo positions regardless of their environment. The directional information of these vectors is used to determine the alignment of halo spins with the LSS.

dynamical properties of the surrounding environment. Filaments and sheets have a preferred direction given by the eigenvector corresponding the single positive or negative eigenvalue. The eigenvectors indicating the direction of the filament as determined from the tidal tensor are shown in Fig. 8. Given these unit eigenvectors $\hat{\boldsymbol{v}}$, we compute the alignment angle $\cos\theta = \hat{\boldsymbol{J}} \cdot \hat{\boldsymbol{v}}$. Fig. 9 shows the median alignment as a function of mass at redshifts $z = 0$, 0.49 and 1.05. At all redshifts, there is a strong tendency for sheet haloes to have a spin vector preferentially parallel to the sheet, i.e. orthogonal to the normal vector. At redshifts up to 0.49, where the error bars of our measurements allow us to investigate trends with halo mass, this alignment increases with increasing mass. For filament haloes, there is a clear trend with halo mass: (i) haloes with masses smaller than about $0.1M_*$ have spins more likely aligned with the filament in which they reside; (ii) haloes in the range $M \approx 0.1M_*$ to $1M_*$ appear to be randomly aligned with respect to the LSS and (iii) for $M \gtrsim M_*$, the trend appears to reverse, and more massive haloes have

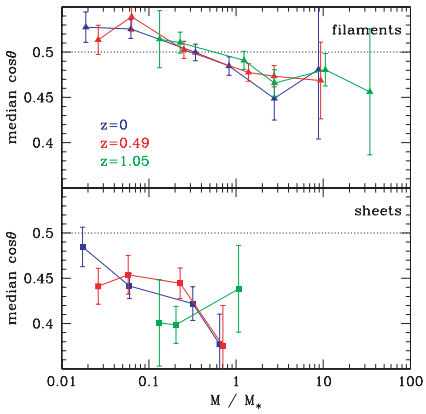

Figure 9. Median alignment angles between the halo angular momentum vectors and the eigenvectors pointing in the direction of filaments and normal to the sheets, respectively. Different redshifts are indicated with the three colours. Error bars indicate the error in the median. The dotted line indicates the expectation value for a random signal.

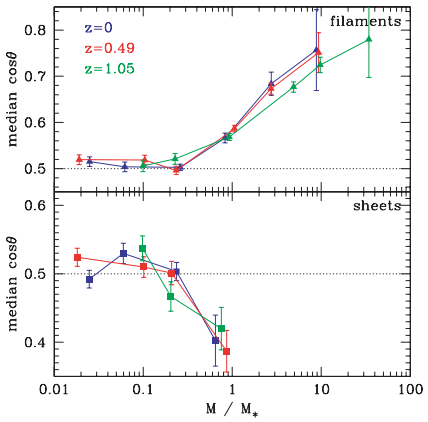

Figure 10. Median alignment angles between the halo major axis vectors and the eigenvectors pointing in the direction of filaments and normal to the sheets, respectively. Different redshifts are indicated with the three colours. Error bars indicate the error in the median. The dotted line indicates the expectation value for a random signal. Data are shown for the ratio of the smoothing scale M_s/M_* fixed.

a weak tendency to spin orthogonally to the direction of the filament at lower redshifts.[1]

To further explore possible connections between the alignment of the LSS and the intrinsic alignment of haloes in the different environments, we search for a correlation signal between the LSS and the axis vectors of the moment of inertia ellipsoid of the haloes. In particular, we use the major axis vector $\boldsymbol{l}_1$ to define the alignment angle $\cos\theta = \hat{\boldsymbol{l}}_1 \cdot \hat{\boldsymbol{v}}$, where $\boldsymbol{v}$ is again the eigenvector normal to a sheet or parallel to a filament. The resulting median correlation is shown in Fig. 10. We find no alignment for halo masses $M < 0.1M_*$; however, in both the filaments and the sheets, the halo major axis appears to be strongly aligned with the LSS for masses above about a tenth of M_*. The strength of the alignment grows with increasing mass. This is possibly to be expected, especially for the most massive haloes, since their shape might influence the potential from which the eigenvectors are derived. Adopting a fixed smoothing scale M_s results merely in a shift of the relations shown in Fig. 10.

Results similar to ours concerning the alignments of shapes and spins with the LSS, and the transition of alignment orientation at M_* in the filaments, are reported by Aragón-Calvo et al. (2007) for $z = 0$ haloes using a definition of environment that is based on density rather than, as in our case, on the gravitational potential, as well as for haloes in the vicinity of clusters by Basilakos et al. (2006) using the moment of inertia ellipsoid of superclusters and by Ragone-Figueroa & Plionis (2007) defining environment by the distance to the nearest cluster. It is clear from our present analysis that such alignments are in place at redshifts of order one, and are maintained virtually unchanged over the last eight or more billion years of evolution of structure in the universe.

[1] The tendency for haloes above M_* to spin orthogonal to the host filament, shown in Fig. 9 for the $M_s/M_* = $ const. smoothing case, is enhanced when the $M_s = $ const. smoothing is adopted. The smoothing scale not only determines the environmental split of the halo population, but also affects the scale on which the eigenvectors of the tidal field are computed. When the smoothing is performed with $M_s/M_* = $ const., the filament direction is obtained on increasingly smaller comoving scales at higher redshifts. This partially erases the stronger correlation that is observed for the most massive haloes when the smoothing is kept at constant comoving scale for all redshifts.

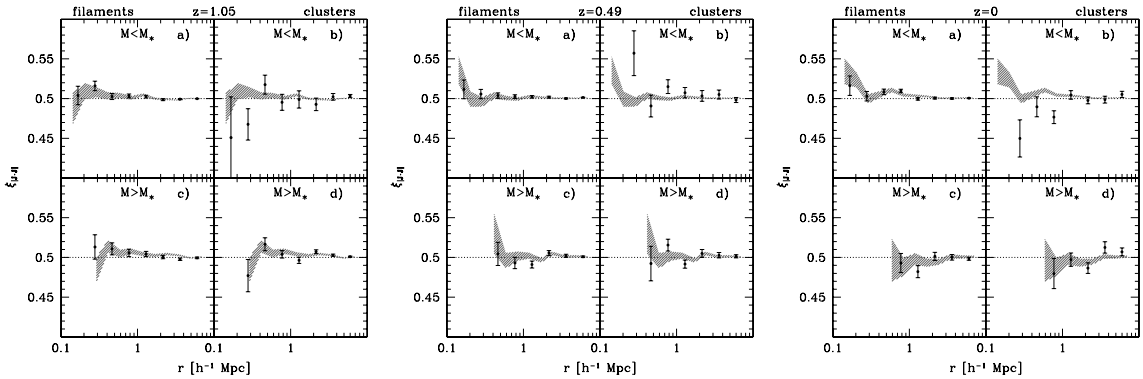

Figure 11. The mean alignment of intrinsic spin angular momentum between haloes in filaments and clusters at redshifts $z = 1.05$ (left), $z = 0.49$ (centre) and $z = 0$ (right). Data for filaments are shown in panels (a) and (c), clusters in panels (b) and (d). The upper panels (a) and (b) show the results for halo masses $M < M_*$, and the lower panels (c) and (d) for halo masses $M > M_*$. The dotted line indicates the expectation value for a random uncorrelated signal. The shaded region indicates the 1σ confidence interval on the mean for the whole sample, split by mass but not split by environment.

3.5.2 Halo–halo alignments

We finally compute the spin–spin and spin–orbit correlation functions using the definitions of Porciani, Dekel & Hoffman (2002) and Bailin & Steinmetz (2005). While we show the results for the $M_s/M_* = $ const. smoothing case, we stress that qualitatively the results remain unchanged when the constant smoothing is adopted.

For the spin–spin correlation we have

$$\xi_{\boldsymbol{J}\cdot\boldsymbol{J}}(r) = \langle\, |\hat{\boldsymbol{J}}(\mathbf{x}) \cdot \hat{\boldsymbol{J}}(\mathbf{x}+\mathbf{r})|\,\rangle, \tag{12}$$

where $\boldsymbol{J}$ is the intrinsic angular momentum of each halo, and the average is taken over all pairs of haloes which are separated by a distance r and reside in the same environment class. Similarly, the spin–orbit correlation is defined as

$$\xi_{\boldsymbol{J}\cdot\boldsymbol{L}}(r) = \langle \hat{\boldsymbol{J}}(\mathbf{x}) \cdot \hat{\boldsymbol{L}}(\mathbf{x}+\mathbf{r})\rangle, \tag{13}$$

where $\boldsymbol{L}$ is the relative orbital angular momentum between two haloes separated by a distance r.

Fig. 11 shows the spin–spin alignment for haloes in clusters and filaments at the three redshifts of our study; upper and lower panels show, respectively, the results for haloes with masses below and above M_*. The shaded region shows the 1σ-confidence area for the total sample, split by mass but not split by environment. The correlations within either of the environmental classes is never stronger than those for the total sample and all of them are consistent with no signal within 2σ. Furthermore, we find no evidence for any significant redshift evolution of these correlations.

The spin–orbit correlation function is shown in Fig. 12. The strong correlation that we found at $z = 0$ in Paper I, extending out to several Mpc, is present also out to redshift $z = 1$ with no significant changes.

4 SUMMARY AND CONCLUSIONS

We have used three N-body simulations, tailored to cover a range of almost five decades in mass with high-resolution haloes (>300 particles), to investigate the dependence of halo shape, spin, formation redshift and alignment as a function of mass, environment and redshift. Using the tidal stability criterion of Paper I we have classified haloes to reside in four different environments: clusters, filaments, sheets and voids. The attribution of haloes to these environments depends on one free parameter, R_s, the length scale used to smooth the underlying mass distribution. Relating this length scale to the mass contained in the Gaussian filter, M_s, in Paper I we optimized by visual inspection the redshift zero value of $M_s = 10^{13}\,h^{-1}\,\mathrm{M}_\odot \approx 2M_*(0)$, with $M_*(z)$ the typical mass scale collapsing gravitationally at redshift z. At the higher redshifts that we study in this paper, we discuss two possible choices for the smoothing mass scale: (i) a smoothing scale constant with redshift and (ii) a smoothing scale that varies such that M_s/M_* remains constant with redshift. The first approach leads to the median overdensity in each environment

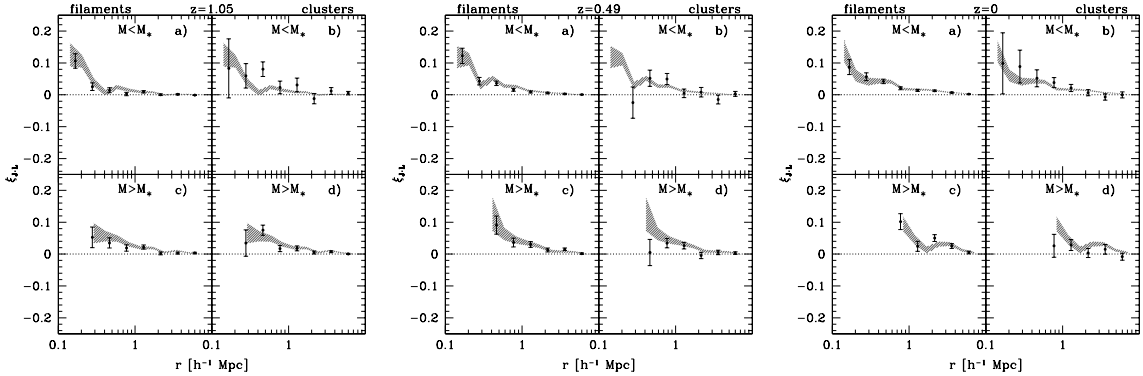

Figure 12. The mean alignment of intrinsic spin and relative orbital angular momentum between haloes in filaments and clusters at redshifts $z = 1.05$ (left), $z = 0.49$ (centre) and $z = 0$ (right). Data for filaments are shown in panels (a) and (c), clusters in panels (b) and (d). The upper panels (a) and (b) show the results for halo masses $M < M_*$, and the lower panels (c) and (d) for halo masses $M > M_*$. The dotted line indicates the expectation value for a random uncorrelated signal. The shaded region indicates the 1σ confidence interval on the mean for the whole sample, split by mass but not split by environment.

increasing just as expected from non-linear enhancement of density fluctuations; the second approach maintains the median density in each environment constant with redshift.

In our analysis of the redshift evolution of the halo properties we find that, when adopting a constant ratio M_s/M_* for the smoothing, the environmental influence is roughly invariant with redshift so that the mass scale at which the environmental influence sets in is roughly given by the mass scale M_*. Unveiling the importance of this physical mass scale in the onset of an environmental dependence of the halo properties is a first step towards understanding the origin of the environmental role in the evolution of dark matter haloes.

Adopting the physically motivated $M_s/M_* = \text{const.}$ smoothing at all redshifts, we have investigated the dependence of the properties of isolated dark matter haloes of masses below and above the M_* threshold on their environment. In general, we find that all halo properties show some dependence on environment for halo masses $M \lesssim M_*$. The strength of the correlations, however, does not change much with redshift. There is virtually no redshift evolution of the halo properties when the correlations with halo mass are expressed in terms of the normalized mass M/M_*, indicating that the strongest evolution with redshift is related to the evolution of the mass scale for collapse, M_*. In detail, our main results are summarized as follows,

(i) There is a strong environmental dependence of halo formation times with environment for haloes with masses $M \lesssim M_*$. At any given mass in this mass regime, haloes in clusters tend to be older than haloes in the other environments, and haloes in voids form much more recently than in any other environment. The global halo population (with no splitting for environment) is well described by a logarithmic relation between mass and formation redshift with a roughly constant slope with redshift.

(ii) The median spin parameter $\lambda'_{\rm med}$ of the total halo sample, not split by environment, increases weakly with mass up to around $10M_*$ at all redshifts. There is no significant residual dependence on redshift besides the mass rescaling with M_*. There is an additional tendency for high-mass haloes in filaments to spin more rapidly than haloes of the same mass in clusters. Haloes in voids have the lowest median spin parameters.

(iii) Haloes of a given ratio M/M_* have very similar median shape parameters independent of redshift in the mass and redshift ranges that we have investigated. Independent of environment, haloes are increasingly more spherical and less triaxial the lower their mass. Haloes with masses $M \lesssim M_*$ are slightly more spherical and more oblate in clusters than in filaments, and there is a hint that the situation reverses for $M \gtrsim M_*$, i.e. that haloes in filaments are more oblate than cluster haloes at high masses. Low-mass haloes in voids have systematically the lowest median sphericity of similar mass haloes in denser environments.

(iv) In the $M \lesssim M_*$ mass regime, haloes in sheets tend to have spin vectors in the plane of the sheets, and haloes in filaments tend to have spin vectors pointing along the filaments; above the M_* mass scale, there is evidence that haloes in filaments reverse the previous trend and tend to have spins orthogonal to the filaments. Furthermore, haloes with masses $M > 0.1M_*$ tend to have their major axis parallel to their host sheets or filaments, with the strength of the alignment increasing with increasing mass. This may reflect the fact that, for massive haloes, the gravitational potential field is substantially influenced by their shape and thus leads to an aligned tidal field. The alignment of halo spins and major axes with the LSS that we have unveiled up to redshifts of order $z = 1$ should be taken into account in studies of weak lensing maps of cosmic shear (e.g. Catelan, Kamionkowski & Blandford 2001), especially in sheets and thus in regions surrounding voids.

(v) There is no evidence for a significant spin–spin correlation between neighbouring haloes. There is in contrast a substantial halo spin–orbit alignment, whose strength appears to be independent of mass, environment and redshift up to $z \sim 1$: haloes in close pairs tend to spin preferentially parallel to the orbital angular momentum of the pair.

An important conclusion that we draw from our study is that the environmental influence on halo properties shows an intriguing dependence on the halo mass, and appears to be essentially modulated by the typical mass scale of gravitational collapse M_* at each redshift. Our data suggest that the $M = M_*(z)$ mass scale might indeed play the role of a *bifurcation point* below which many of the median properties of dark matter haloes either begin to feel the influence of their large-scale environment, or show an opposite response to their large-scale environment relative to the more massive haloes. The existence of such a thresholding mass scale in the environment–halo relationship is yet to be understood.

ACKNOWLEDGMENTS

OH acknowledges support from the Swiss National Science Foundation. All simulations were performed on the Gonzales cluster at ETH Zurich, Switzerland.

REFERENCES

Allgood B., Flores R. A., Primack J. R., Kravtsov A. V., Wechsler R. H., Faltenbacher A., Bullock J. S., 2006, MNRAS, 367, 1781
Aragón-Calvo M. A., van de Weygaert R., Jones B. J. T., van der Hulst J. M., 2007, ApJ, 655, L5
Avila-Reese V., Colín P., Gottlöber S., Firmani C., Maulbetsch C., 2005, ApJ, 634, 51
Bailin J., Steinmetz M., 2005, ApJ, 627, 647
Basilakos S., Plionis M., Yepes G., Gottlöber S., Turchaninov V., 2006, MNRAS, 365, 539
Bertschinger E., 2001, ApJS, 137, 1
Bett P., Eke V., Frenk C. S., Jenkins A., Helly J., Navarro J., 2007, MNRAS, 376, 215
Blanton M. R., Eisenstein D., Hogg D. W., Schlegel D. J., Brinkmann J., 2005, ApJ, 629, 143
Bond J. R., Cole S., Efstathiou G., Kaiser N., 1991, ApJ, 379, 440
Bryan G. L., Norman M. L., 1998, ApJ, 495, 80
Bullock J. S., Dekel A., Kolatt T. S., Kravtsov A. V., Klypin A. A., Porciani C., Primack J. R., 2001, ApJ, 555, 240
Catelan P., Kamionkowski M., Blandford R. D., 2001, MNRAS, 320, L7
Croton D. J., Gao L., White S. D. M., 2007, MNRAS, 374, 1303
Davis M., Efstathiou G., Frenk C. S., White S. D. M., 1985, ApJ, 292, 371
Doroshkevich A. G., 1970, Astrophysics, 6, 320
Dressler A., 1980, ApJ, 236, 351
Eke V. R., Cole S., Frenk C. S., 1996, MNRAS, 282, 263
Gao L., White S. D. M., 2007, MNRAS, 377, L5
Gao L., Springel V., White S. D. M., 2005, MNRAS, 363, L66
Hahn O., Porciani C., Carollo C. M., Dekel A., 2007, MNRAS, 375, 489 (Paper I)
Harker G., Cole S., Helly J., Frenk C., Jenkins A., 2006, MNRAS, 367, 1039
Hetznecker H., Burkert A., 2006, MNRAS, 370, 1905
Kauffmann G., White S. D. M., Heckman T. M., Ménard B., Brinchmann J., Charlot S., Tremonti C., Brinkmann J., 2004, MNRAS, 353, 713
Lacey C., Cole S., 1993, MNRAS, 262, 627
Macciò A. V., Dutton A. A., van den Bosch F. C., Moore B., Potter D., Stadel J., 2007, MNRAS, 378, 55
Maulbetsch C., Avila-Reese V., Colín P., Gottlöber S., Khalatyan A., Steinmetz M., 2007, ApJ, 654, 53

Peebles P. J. E., 1969, ApJ, 155, 393
Porciani C., Dekel A., Hoffman Y., 2002, MNRAS, 332, 325
Ragone-Figueroa C., Plionis M., 2007, MNRAS, 377, 1785
Reed D. S., Governato F., Quinn T., Stadel J., Lake G., 2007, MNRAS, 378, 777
Sheth R. K., Tormen G., 2004, MNRAS, 350, 1385
Springel V., 2005, MNRAS, 364, 1105
Vitvitska M., Klypin A. A., Kravtsov A. V., Wechsler R. H., Primack J. R., Bullock J. S., 2002, ApJ, 581, 799
Wang H. Y., Mo H. J., Jing Y. P., 2007, MNRAS, 375, 633
Wechsler R. H., Zentner A. R., Bullock J. S., Kravtsov A. V., Allgood B., 2006, ApJ, 652, 71
Wetzel A. R., Cohn J. D., White M., Holz D. E., Warren M. S., 2007, ApJ, 656, 139
Zel'dovich Y. B., 1970, A&A, 5, 84

This paper has been typeset from a TEX/LATEX file prepared by the author.